Journal of the Mechanical Behavior of Biomedical Materials 105 (2020) 103705

Contents lists available at ScienceDirect

Journal of the Mechanical Behavior of Biomedical Materials

journal homepage: http://www.elsevier.com/locate/jmbbm

Topology optimization of 3D-printed structurally porous cage for acetabular reinforcement in total hip arthroplasty

Ahmed Moussa [a,1], Shakurur Rahman [a,1], Manman Xu [a], Michael Tanzer [b], Damiano Pasini [a,*]

[a] Department of Mechanical Engineering, McGill University, Montreal, Quebec, H3A0C3, Canada
[b] Division of Orthopaedics, Department of Surgery, McGill University, Jo Miller Orthopaedic Research Laboratory, Montreal, Quebec, H3G1A4, Canada

ARTICLE INFO

Keywords:
Pelvis cage
Porous load-bearing biomaterials
Homogenization
Topology optimization
Additive manufacturing
Interfacial stress
Micromotion

ABSTRACT

Aseptic loosening and mechanical failure of acetabular reinforcement components are among the main causes of their reduced service life. Current acetabular implants typically feature a structural solid layer that provides load bearing capacity, coated with a foam of uniform porosity to reduce stress shielding and implant loosening. This paper presents an alternative concept for a 3D printed cage that consists of a multifunctional fully porous layer with graded attributes that integrate both structural function and bone in-growth properties. The design comprises a hemispherical cup affixed to a superior flange with architecture featuring an optimally graded porosity. The methodology here presented combines an upscaling mechanics scheme of lattice materials with density-based topology optimization, and includes additive manufacturing constraints and bone ingrowth requirements in the problem formulation. The numerical results indicate a 21.4% reduction in the maximum contact stress on the bone surface, and a 26% decrease in the bone-implant interface peak micromotion, values that are indicative of enhanced bone ingrowth and implant long-term stability.

1. Introduction

Acetabular reinforcement components are essential in restoring proper biomechanical functioning of the hip, following Total Hip Arthroplasty (THA) (Ma et al., 2013). The complexity of acetabular reinforcements amplifies in case of severe bone defects (Paprosky et al., 1994), sub-par bone quality on the bone-implant interface (Ma et al., 2013; Perka and Ludwig, 2001) or considerable proportions of bone grafts on the acetabulum (Pollock and Whiteside, 1992). Several approaches have been proposed for acetabular revisions, such as the use of metallic acetabular rings and cages (Winter et al., 2001; Kawanabe et al., 2007), either cemented (Hirst et al., 1987; Mendes et al., 1984) or cementless (Paprosky et al., 1994; Padgett et al., 1993; Paprosky and Magnus, 1994; Rosson and Schatzker, 1992); a high hip center positioning of the implants (Dearborn and Harris, 1999; Schutzer and Harris, 1994); and the use of jumbo cups (Ito et al., 2003; Hendricks and Harris, 2006; Patel et al., 2003) or triflange cups (Moore et al., 2018). An alternative to these approaches is the Burch-Schneider (BS) reinforcement cage, introduced in the mid-1970s with so far a notable short-term to mid-term success (Hoell et al., 2012). Its structural characteristics provide a large contact area with the pelvic bone, thereby distributing the concentrated load from the femoral head (Hoell et al., 2012). Aseptic loosening, however, has been observed along with mechanical failure in 10.5% of patients over a five-twenty one years' follow-up (Symeonides et al., 2009). Other problems of BS cage have been reported for both septic (3.2%) and aseptic (4.8%) loosening after a mean of 5.45 years (Perka and Ludwig, 2001).

Acetabular cages have been conventionally made of fully-solid biocompatible material, such as titanium alloy (Ti6Al4V) (Dall'Ava et al., 2019), which is typically much stiffer than the host bone tissue. The mismatch in elastic properties between implant and bone tissue results in stress shielding, with the former carrying a significant proportion of the applied load and the latter lacking the adequate mechanical stimuli for its remodeling. This leads to bone resorption, followed by implant loosening and subsequent failure (Huiskes et al., 1992; Katoozian et al., 2001). To circumvent stress shielding, flexible composite implants have been used, but their success rate is very low mainly due to micromotion leading to bone-implant interface debonding (Huiskes et al., 1992; Katoozian et al., 2001). Other strategies employ the use of a porous coating not only to facilitate bone ingrowth, but also to improve biological fixation and reduce later-stage micromotion (Jasty et al., 1997; Levine, 2008; Bose et al., 2013). These porous coatings,

* Corresponding author.
E-mail address: damiano.pasini@mcgill.ca (D. Pasini).
[1] Equal contribution.

https://doi.org/10.1016/j.jmbbm.2020.103705
Received 19 November 2019; Received in revised form 7 February 2020; Accepted 16 February 2020
Available online 24 February 2020
1751-6161/

however, have uniform porosity and very low mechanical strength due to their stochastic arrangement of compliant unit cells. On the contrary, porous architected biomaterials with load bearing unit cells have the advantage of providing high tunability of their morphological parameters (cell topology, nodal connectivity and porosity), so as to enhance mechanical properties and biomechanical performance (Arabnejad et al., 2016, 2017; Bobyn et al., 1980, 1999).

Architected porous biomaterials can be designed to improve performance and functionality of current orthopaedic implants (Arabnejad et al., 2017; Arabnejad Khanoki and Pasini, 2012; Moussa et al., 2018; Rahimizadeh et al., 2018; Lin et al., 2004; Fraldi et al., 2010; Abbas et al., 2018; Al-Tamimi et al., 2017). Their unit cell topology along with its characteristic morphological parameters (e.g. pore size and shape) can be selected to realize an optimal combination of structural and functional properties, hence by-passing any trial-and-error approach (Dall'Ava et al., 2019). In addition, the distribution of their mechanical properties can be systematically tailored through structural optimization to generate complex architecture that can be built almost with no restrictions via additive manufacturing (AM), such as selective laser melting (SLM), selective laser sintering (SLS), or electron beam melting (EBM) (Wang et al., 2016; Murr et al., 2010; Sobral et al., 2011). In reality, however, AM poses manufacturing limits on architected materials that are built with geometric features at the resolution limit of current technology, an outcome that can impact mechanical properties, bone ingrowth and other implant functions.

Current acetabular implants in the market generally consists of a cup with a stochastic and periodic porous coating (Dall'Ava et al., 2019) that has no load bearing function. Their uniform porosity contributes minimally to the reduction of stress shielding and it gives no control over the stress levels and micromotion at the bone-implant interface. In contrast, minimizing stress levels would provide an ideal environment for the host bone healing and bone graft remodeling prior to bone ingrowth (Gross and Goodman, 2005; Kawanabe et al., 2011; Sembrano and Cheng, 2008); and lowering levels of micromotion at the early stage would directly contribute to bone ingrowth (Perona et al., 1992; Kienapfel et al., 1999).

This paper introduces the design of a cementless porous acetabular reinforcement implant whose architecture is conceived to provide both load bearing capacity and bone ingrowth. Devised with the clinical guidance of an orthopedic surgeon for primary and revision hip surgeries, its macro-geometry consists of a hemispherical cup attached to a superior flange, characteristics that improve cage stability in the pelvic bone. A density-based topology optimization is used to tailor the elastic properties of its inner porous architecture via compliance minimization, which ensures the necessary stiffness and load bearing capacity required by an implant with thin depth. The method allows generating a graded porosity distribution that reduces bone-implant interface stress intensity and micromotion, the latter expected to reduce the probability of aseptic loosening in the long-term. Bone ingrowth and additive manufacturing constraints are systematically introduced in the problem formulation, as described in Section 2. Results of stress levels and micromotion are given in Section 3 and compared with those of two baselines, a fully-solid counterpart and another fully-porous one but with uniform porosity distribution. A discussion of the limitations of the current design follows, along with a set of recommendations for future improvements.

2. Methodology

Our goal here is to develop a 3D printed porous cementless acetabular reinforcement cage with tailored elastic modulus resulting in an optimally graded porosity distribution that can achieve a primary and secondary goal. The former is to provide load bearing capacity and sufficient bone ingrowth, and the latter is to reduce contact stress intensity and micromotion, two critical bottlenecks of current pelvis implants which are fully solid with uniform mechanical properties. The macro-geometry of our implant design consists of a perfectly hemispherical cup for the acetabulum and a flange that rests on the ilium of the pelvic bone. This distributes the load from the femoral head into a large surface area. The implant has screw holes on both the cup and the flange for stable fixation until bone ingrowth occurs. The numerical model here consists of an assembly of components: femoral head, liner, solid layer, fully-porous structural layer and the pelvic bone. The focus of this work is on the fully-porous layer. Topology optimization is used to generate a graded porosity distribution with tuned elastic properties, expressed as a function of relative density. Anatomical boundary conditions as well as clinical (both porosity and bone ingrowth) and additive manufacturing constraints are included in the problem formulation.

The combination of multi-scale mechanics and density-based topology optimization underlies the conceptual framework underpinning this work. While a methodology has been developed to design knee and vertebral implants addressing the specific clinical and structural requirements of their application (Moussa et al., 2018; Rahimizadeh et al., 2018), this work extends it to cope with the design of a load bearing pelvis cage which poses its own design requirements. The method allows to generate a structural porous implant that differs substantially from the fully solid cage implants currently available in the orthopedic market. Fig. 1 illustrates the steps summarized below:

- *Adoption of pelvic bone geometry and assignment of elastic properties.* 1877 computed tomography (CT) scan images of a 38-year-old male are obtained from the Visible Human Project (VHP) database of the US National Library of Medicine. The three-dimensional (3D) model of the pelvis is created from the CT scans and assembled with 3D models of the implant, liner and femoral head for the numerical analysis. The Hounsfield Unit values (HU) of the CT scan voxels are used to assign elastic properties to the 3D model of the bone.
- *Choice of unit cell geometry.* An open cell, tetrahedron-based unit cell topology is used as the building block of the porous implant. Its topology is stretch-dominated; it offers load bearing capabilities and enables bone ingrowth (Arabnejad et al., 2016; Melancon et al., 2017). Asymptotic homogenization is used under the assumption of length scale separation between unit cell and implant geometry, to calculate the elastic constants of the unit cell as a function of its relative density (Hassani and Hinton, 1998; Hollister and Kikuchi, 1992; Khanoki and Pasini, 2013; Arabnejad and Pasini, 2013; Fang et al., 2005).
- *Finite Element Analysis (FEA).* An initial, uniform relative density distribution is assigned to the implant and prescribed loading and boundary conditions are applied to the 3D assembly. The applied load consists of the forces experienced by the pelvis during one-legged standing. Distributions of stress, strain, strain energy and displacement are obtained from the numerical results for the pelvis as well as the implant.
- *Topology Optimization.* Due to the very low thickness of the implant, the topology optimization is solved for minimum strain energy, to ensure the necessary load bearing capacity. The relative density ρ of each element is the design variable, which is updated by using the Method of Moving Asymptotes (MMA) (Svanberg, 1987). The unit cell homogenized properties and the nodal displacements of each mesh element are used to construct the global stiffness tensor. The gradient of the objective function is calculated by partially taking the derivatives of the stiffness tensor components with respect to the relative density. The compliance of the implant is minimized until an optimized distribution of relative density is achieved.

2.1. Numerical model

Data from 1877 computed tomography (CT) scan images of a 38-year-old male, weighing 80 kg, are used to create the three-dimensional (3D) model of the pelvic bone. The CT scan slice spacing is 1 mm and the pixel size in each image is 0.9375 mm. A semi-automatic

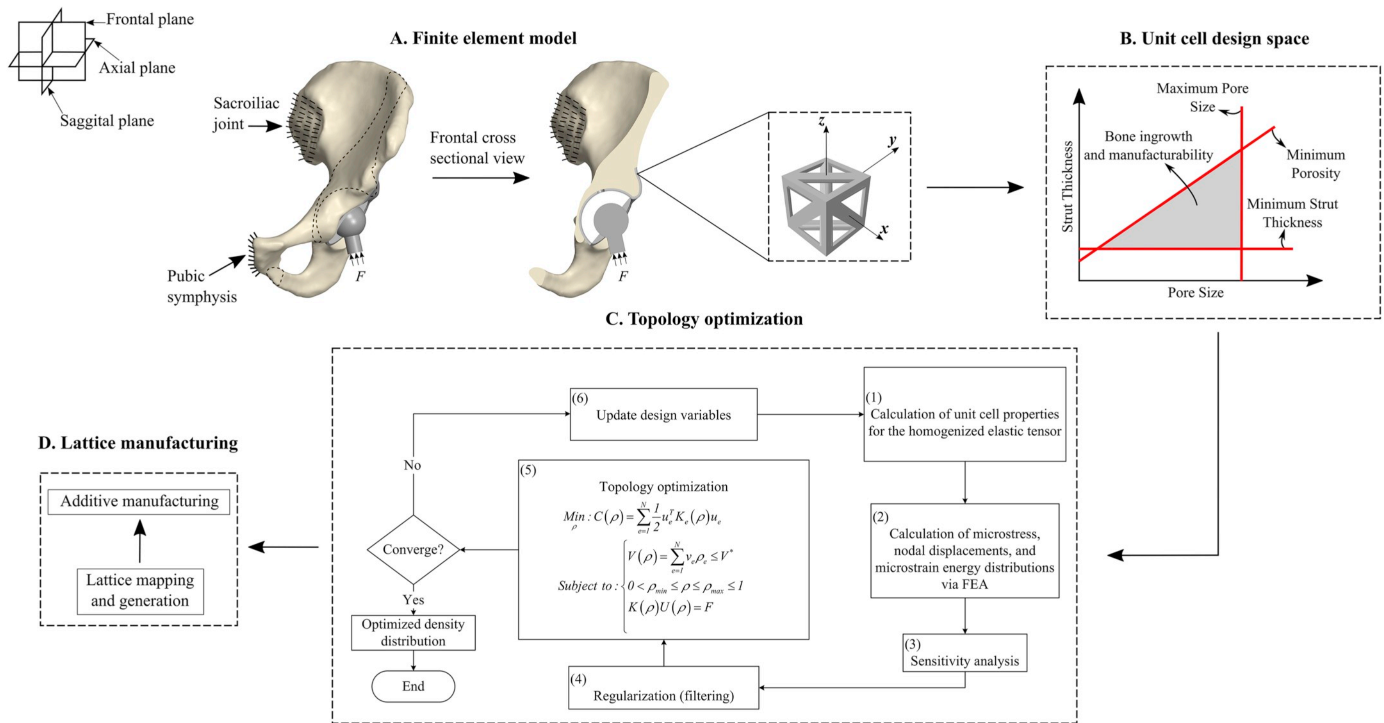

Fig. 1. (A) Finite element model of implanted pelvis, liner and femoral head assembly with applied loading and boundary conditions; (B) Admissible design space for tetrahedron-based unit cell, accounting for bone ingrowth (pore size and porosity) and additive manufacturing (strut thickness) constraints; (C) Sub-flow chart depicting the homogenized scheme and topology optimization to generate the graded porosity of the pelvis cage; (D) Lattice generation and additive manufacturing of the implant.

segmentation is performed on the CT scan images using ITK-SNAP (Yushkevich et al., 2006) to produce the bone geometry. The Stereo-Lithography (STL) format mesh file is exported to MeshLab (Cignoni et al., 2008) to generate a point cloud file from the volume mesh. SolidWorks® (Dassault Systèmes SolidWorks Corporation, Waltham, Massachusetts, USA) is then used to create the 3D computer-aided design (CAD) model from the point cloud file. The CAD models for the implant, liner and femoral head are also created using SolidWorks®. The superior flange of the implant that rests on the ilium of the pelvic bone is created from the surface of the bone itself and augmented with a perfectly hemispherical cup. Screw holes are added on both the flange and the cup to provide structural fixation. The location and size of the screw holes on the cup replicate those in the Trident® Tritanium™ Acetabular System (Stryker Corporation, Kalamazoo, Michigan, USA), currently available in the market. The implant, liner and femoral head are assembled with the bone. A groove is created on the bone surface on which the implant rests. This mimics the surgical protocol and ensures proper contact between the bone and the implant. The volume mesh of the assembly is created in Altair HyperWorks® (Troy, Michigan, USA) using ten-node second-order tetrahedron elements. The choice of the mesh element ensures successful meshing of complex geometries with reasonable element quality (Yang, 2017). Finally, the mesh file is exported to ANSYS® (Canonsburg, Pennsylvania, USA).

The next step in the analysis involves assigning the appropriate material properties to the 3D numerical assembly. From the CT scan data, the significant contrast between hard and soft tissues is used to assign the material properties of the bone (Peng et al., 2006; Viceconti et al., 1998; Odgaard, 1997; Lengsfeld et al., 1998). The CT number, known as the Hounsfield Unit (HU) value of each voxel, is assumed linearly proportional to the bone mineral density (BMD) (Crawford et al., 2003; Rho et al., 1995; Leung et al., 2009; Iqbal et al., 2019). This relationship between HU value and BMD can be used to calculate the elastic properties of bone tissue (Peng et al., 2006; Rho et al., 1995; Leung et al., 2009; Iqbal et al., 2019).

The bone tissue of the pelvis is heterogeneous, consisting of mainly cortical and cancellous bones, each corresponding to a specific HU in the CT scan data (Leung et al., 2009). The HU of each node is first assigned from the nearest CT sampling point. The HU of each element is then calculated by averaging the nodal HU values (Moussa et al., 2018; Peng et al., 2006). The apparent bone mineral density ρ_B of each element is thereupon determined from the corresponding HU values. From previous studies (Leung et al., 2009; Iqbal et al., 2019), the bone mineral density ρ_B of the pelvic bone, as a function of HU, can be shown as:

$$\rho_B = 6.9141 \times 10^{-4} \times HU + 1.026716 \tag{1}$$

Subsequently, the elastic properties of each mesh element of the bone can be directly calculated from ρ_B. The relation between elastic properties and BMD varies with anatomical position (Leung et al., 2009; Morgan et al., 2003). Assuming isotropic linear elastic properties, an empirical relationship is here adopted for the pelvic bone (Leung et al., 2009; Dalstra et al., 1993):

$$E = 2017.3\rho_B^{2.46} \tag{2}$$

where, E is the Young's modulus in MPa and ρ_B is the bone mineral density in g/cm^3; while, the Poisson's ratio ν has been selected to be 0.3. However, due to partial volume effect from reading HU values, the elastic properties of the surface elements, comprising the cortical bone only, are generally underestimated; hence, the Young's modulus of the cortical bone elements are assumed constant at 17 GPa (Leung et al., 2009; Dalstra et al., 1995). This completes the material property assignment for the pelvis mesh elements, with the elastic modulus ranging from 6.49 GPa to 17 GPa and the Poisson's ratio constant at 0.3.

Ti6Al4V is a titanium alloy (Dall'Ava et al., 2019) with biocompatibility, desirable mechanical properties and corrosion resistance necessary for orthopedic implants. It is used here for the implant and the femoral head, whereas polyethylene is selected for the liner. Both materials are assumed isotropic. The material properties of heat-treated, additively manufactured Ti6Al4V are E = 114 GPa and ν = 0.349 (Melancon et al., 2017). The elastic properties of polyethylene are E = 945 MPa and $\nu = 0.45$. The choice of the material properties for Ti6Al4V further incorporates additive manufacturing considerations into the implant design.

As per the boundary conditions, the human pelvis is constrained by joints as well as a complex network of ligaments. Several simplifications are suggested in the literature (Hao et al., 2011); and, in this work, only the pubic symphysis and sacroiliac joint are constrained to be fixed in all degrees of freedom. Also, for the purpose of this study, the load is selected to be applied at 250% of the body weight, resulting in a force of 1962N for a patient weighing 80 kg (Kawanabe et al., 2011). A safety factor of 2 is additionally used for the load to produce a more conservative design (Lin et al., 2004). This compressive load is applied through the femoral head stem, inclined at 78° with the horizontal/axial plane (Kawanabe et al., 2011). Finally, frictionless, bonded contact conditions are applied to the respective contact interfaces.

2.2. Homogenized material properties of the implant

A detailed finite element analysis of a fully-porous implant is computationally expensive, but it can be circumvented by assuming the implant to be a homogenized medium (Arabnejad and Pasini, 2013). This enables the use of a unit cell as a representative volume element (RVE), the effective properties of which is 'representative' of the porous implant. The theory of asymptotic homogenization (AH) (Hollister and Kikuchi, 1992) is used to compute the effective elastic properties of the RVE, which can be used to assemble the global stiffness tensor of the implant. This homogenization approach has been widely used in previous studies for orthopedic implants (Arabnejad et al., 2017; Moussa et al., 2018; Rahimizadeh et al., 2018; Wang et al., 2018); hence, only a brief discussion is reported here.

By solving a problem formulated locally on the RVE, the effective stiffness tensor of the porous unit cell, E^H_{ijkl}, can be calculated as (Hollister and Kikuchi, 1992):

$$E^H_{ijkl} = \frac{1}{|Y|}\int_{Y_s} E_{ijpm} M_{pmkl} dY \tag{3}$$

Here, $|Y|$ is the total unit cell volume, including the void space; Y_s corresponds to the solid material of the unit cell only and E_{ijpm} is the local stiffness tensor, the value of which spans from zero to the bulk material elastic tensor itself, corresponding to the voids and the solid materials respectively. Additionally, a local structure tensor, M_{ijkl}, is defined that relates the local macro-strain, $\bar{\varepsilon}_{kl}$, to the local micro-strain, ε_{ij} as follows (Hollister and Kikuchi, 1992):

$$\varepsilon_{ij} = M_{ijkl}\bar{\varepsilon}_{kl} \tag{4}$$

$$M_{ijkl} = \frac{1}{2}\left(\delta_{ik}\delta_{jl} + \delta_{il}\delta_{jk}\right) - \varepsilon^{*\ kl}_{ij} \tag{5}$$

Here, δ_{ij} is the Kronecker delta, and $\varepsilon^{*\ kl}_{ij}$ is the microscopic strain corresponding to the component kl of the macroscopic stain. Assuming small deformation and linear elasticity, $\varepsilon^{*\ kl}_{ij}$ is calculated by solving a problem formulated locally on the RVE as (Hollister and Kikuchi, 1992):

$$\int_{Y_s} E_{ijpm}\varepsilon^1_{ij}(v)\varepsilon^{*\ kl}_{pm}(u)\ \ dY = \int_{Y_s} E_{ijkl}\varepsilon^1_{ij}(v)\bar{\varepsilon}_{kl}\ \ dY \tag{6}$$

with, $\varepsilon^1_{ij}(v)$ as the virtual strain.

In three dimensions, six arbitrary unit strains are required to construct M_{ijkl}. By applying periodic boundary conditions on the edges of the RVE, the periodicity of the strain field and equal nodal displacements on the opposite edges are ensured (Hollister and Kikuchi, 1992; Hassani, 1996). With M_{ijkl} being computed, the homogenized stiffness tensor of the unit cell, E^H_{ijkl}, is calculated using (3) (Arabnejad et al., 2017; Arabnejad Khanoki and Pasini, 2012; Hollister and Kikuchi, 1992).

This procedure is used to calculate the effective elastic properties of the tetrahedron-based unit cell at given values of relative density. The tetrahedron-based unit cell has six independent elastic constants expressed in terms of Young's modulus, shear modulus and Poisson's ratio (Melancon et al., 2017). The effective elastic moduli normalized with the corresponding properties of the bulk solid is plotted as a function of relative density ρ in Fig. 2.

2.3. Topology optimization

Density-based topology optimization is used to optimize material distribution within the porous domain of the implant (Bendsøe and Sigmund, 2003). Asymptotic homogenization is used to express the elastic properties of the porous implant as a function of relative density, as described in Section 2.2. The allowable relative density range is constrained, subjected to bone ingrowth and additive manufacturing requirements, and the elastic properties are optimized to enhance the functional performance of the implant.

2.3.1. Bone ingrowth and manufacturing constraints

To ensure clinical functionality and manufacturability via additive manufacturing, the porous domain of the implant must be optimized, subjected to bone ingrowth and manufacturing constraints. A previous study characterized the interplay between bone ingrowth and manufacturing constraints, which effectively translates into a constraint on the allowable range of relative densities of the unit cell (Melancon et al., 2017). Two unit cell topologies were examined, tetrahedron-based and octet-truss, because of their high-strength topology stemming from their stretch-dominated behaviour. For bone ingrowth to occur, the pore size of the unit cell has to be between 50 μm and 650 μm and the porosity is required to be over 50%; while for manufacturability, the minimum allowable strut thickness is 200 μm. This translates into an allowable design space with upper and lower bounds on the relative density for a given choice of unit cell size, relations that account for both bone ingrowth and manufacturing constraints. Validated through a campaign of experiments, these design maps are specific to a given unit cell topology, and provide knockdown factors that guide the elastic and yield strength design of high-strength porous biomaterials (Arabnejad et al., 2016; Melancon et al., 2017). For this work, a tetrahedron-based unit cell of 1.5 mm is chosen. Within the admissible design space that it results, a relative density range of 0.3–0.5 is selected as the design variable

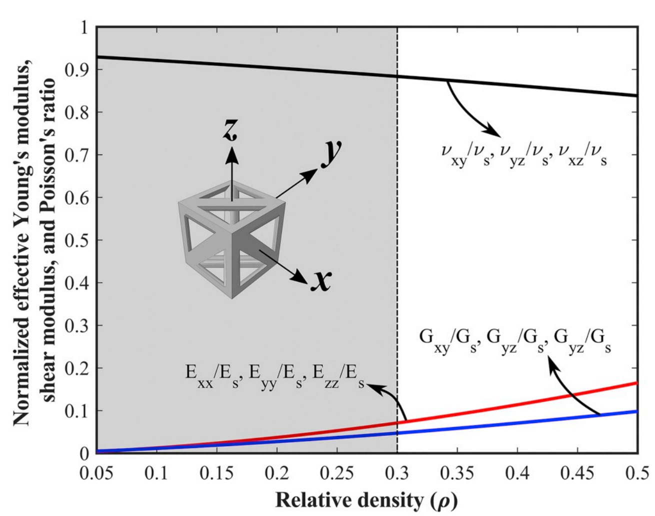

Fig. 2. Normalized effective properties of the tetrahedron-based unit cell as a function of the relative density. From the admissible design space, the relative density range is selected to be from 0.3 to 0.5, as indicated by the white region.

range for the optimization framework, and the mean value of 0.4 is selected as the volume fraction constraint to allow for the generation of optimum gradients in porosity. This results in approximately 89% decrease in Young's modulus (Fig. 2) from 114 GPa (fully solid) to 12.54 GPa (fully porous).

2.3.2. Problem formulation and sensitivity analysis

Topology optimization is solved for minimum compliance to ensure sufficient load bearing capacity of the porous implant with very low thickness. The numerical scheme tailors the elastic properties of the implant and, thereby, reduces the stiffness mismatch with the bone. This lowers the stress levels and micromotion at the bone-implant interface and ensures appropriate bone ingrowth while maintaining load bearing capacity.

With the relative density ρ as the design variable, the optimization problem can be stated as:

$$\underset{\rho}{\text{Min}} : C(\rho) = \frac{1}{2}F^T U(\rho) = \sum_{e=1}^{N} \frac{1}{2} u_e^T K_e(\rho) u_e$$

$$\textit{Subject to}: \begin{cases} V(\rho) = \sum_{e=1}^{N} v_e \rho_e \leq V^* \\ 0 < \rho_{\min} \leq \rho \leq \rho_{\max} \leq 1 \\ K(\rho)U(\rho) = F \end{cases} \tag{7}$$

where, C is the compliance of the implant, F is the global force vector applied to the implant, $U(\rho)$ is the global nodal displacement vector, K is the global stiffness matrix of the implant, ρ is the vector of relative densities, ρ_e is the relative density of each element e, V^* is the prescribed volume fraction of solid material, ν_e is the volume of each element and N is the total number of elements. Here, $\rho_{\min} = 0.3$ and $\rho_{\max} = 0.5$, while V^* is selected to be 0.4 (refer to Section 2.3.1).

The density filter (Bruns and Tortorelli, 2001) is implemented here, as it helps avoid numerical instabilities and mesh dependency, and also ensures manufacturability:

$$\tilde{\rho}_e = \frac{\sum_{i \in N_e} w(x_i) v_i \rho_i}{\sum_{i \in N_e} w(x_i) v_i} \tag{8}$$

Here, $\tilde{\rho}_e$ is the filtered relative density of element e, ν_i is the volume of element i, N_e corresponds to the neighborhood elements of element e and $w(x_i)$ is a weighting function defined as:

$$w(x_i) = R - \|x_i - x_e\| \tag{9}$$

where, R is the specified filter radius, x_i and x_e are the coordinates of the center of elements i and e respectively.

Since the sensitivity calculations of minimum compliance topology optimization have been comprehensively reported in the literature (Moussa et al., 2018; Rahimizadeh et al., 2018), it is only briefly discussed here. The derivative of the objective function can be calculated as:

$$\frac{\partial C(\tilde{\rho})}{\partial \rho_e} = \sum_{i=1}^{N_e} \frac{\partial C(\tilde{\rho})}{\partial \tilde{\rho}_i} \frac{\partial \tilde{\rho}_i}{\partial \rho_e} \tag{10}$$

where, the sensitivity of the filtered relative density with respect to the design variable, $(\partial \tilde{\rho}_i / \partial \rho_e)$ can be found as:

$$\frac{\partial \tilde{\rho}_i}{\partial \rho_e} = \frac{w(x_e) v_e}{\sum_{j \in N_i} w(x_j) v_j} \tag{11}$$

The derivative of the objective function with respect to the filtered relative density can be expressed as:

$$\frac{\partial C(\tilde{\rho})}{\partial \tilde{\rho}_i} = -\frac{1}{2} U^T(\tilde{\rho}) \frac{\partial K(\tilde{\rho})}{\partial \tilde{\rho}_i} U(\tilde{\rho}) \tag{12}$$

Here, $\partial K(\tilde{\rho}) / \partial \tilde{\rho}_i$ is the derivative of the homogenized stiffness matrix with respect to the filtered density, which is found for a ten-node quadratic tetrahedral solid element in the *rst* natural coordinate system with five Gauss points as (Moussa et al., 2018; Rahimizadeh et al., 2018):

$$\frac{\partial K_e(\tilde{\rho})}{\partial \tilde{\rho}_e} = \sum_{k=1}^{5} w_k B_{rst}^T(r_k, s_k, t_k) \frac{\partial E^H(\tilde{\rho})}{\partial \tilde{\rho}_e} B_{rst}(r_k, s_k, t_k) \quad |J| \tag{13}$$

where, B is the strain-displacement matrix, E^H is the homogenized elastic tensor of element e as a function of its relative density, J is the Jacobian matrix and w_k is the weight of the Gauss points k.

The sensitivity of the base solid volume of the porous implant $V(\rho)$ with respect to the design variable ρ can be found as:

$$\frac{\partial V(\tilde{\rho})}{\partial \rho_e} = \sum_{i \in N_e} \frac{\partial V(\tilde{\rho})}{\partial \tilde{\rho}_i} \frac{\partial \tilde{\rho}_i}{\partial \rho_e} \tag{14}$$

where,

$$\frac{\partial V(\tilde{\rho})}{\partial \tilde{\rho}_i} = v_s \tag{15}$$

with, ν_s as the volume of the base solid material used in the porous implant.

The sensitivity analysis provides the search direction towards the optimized solution, which is used in the Method of Moving Asymptote (MMA) (Svanberg, 1987) algorithm to update the design variables until convergence is reached.

3. Results and discussion

The methodology explained in Section 2 is applied to design the acetabular cage with a functionally graded fully-porous side on the region of contact with the bone tissue. We start with a description of the optimized architecture and then we discuss the pelvis cage performance, mainly the implant stiffness, which is the objective function of the optimization framework, the contact stress distribution on the bone surface, the micromotion at the bone-implant interface and the structural capacity of the cage to resist the applied loads. Comparisons with results from a corresponding uniform porosity implant and a baseline fully-solid implant are given to assess the performance gain of the implant presented in this work.

Fig. 3 shows the optimized relative density distribution of the functionally graded structurally porous layer of the implant, along with the corresponding porous cage obtained by mapping the density distribution into a tetrahedron-based lattice micro-architecture. The lattice generation is done via an in-house mapping script developed for Rhinoceros 3D (Robert McNeel & Associates, Seattle, Washington, USA) (Wang et al., 2017).

For comparison of the objective function values (Table 1), we calculate the strain energy of the porous optimized implant and a uniform porosity implant for the prescribed value of volume fraction of 0.4 and given loading condition. A lower strain energy implies lower compliance, i.e. higher stiffness; the porous optimized implant shows lower values of the total, average and maximum strain energy compared to its porous uniform counterpart. The same conclusion is also drawn from strain energy density (SED) calculation, with the porous optimized implant showing a lower SED under the same loading condition, which implies higher stiffness than the porous uniform implant. This highlights the benefit of using topology optimization for this application, as a higher stiffness is desired to ensure the necessary load bearing capacity for a reinforcement cage that is very thin. The porous optimized implant also provides lower contact stress and micromotion; such a gain in the

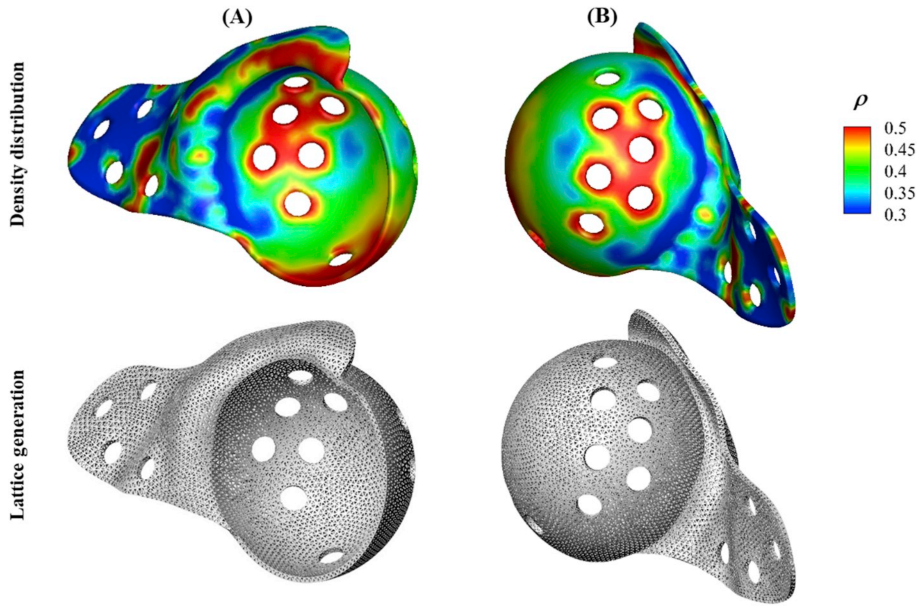

Fig. 3. Optimized relative density distribution of the implant and the corresponding lattice architecture with, (A) front side adjacent to the solid layer and (B) back side adjacent to the bone.

Table 1
Strain energy, contact stress and micromotion for uniform porosity fully-porous and optimized fully-porous implants, with identical solid volume fraction of 0.4. Percentage gains for the optimized implant are also provided.

	Strain energy (J)			Contact stress (MPa)	Micromotion (μm)
	Total	Average	Maximum	Maximum	Maximum
Uniform porosity	0.00418279	1.8212E-07	1.3956E-05	16.6	6.87
Porous optimized	0.0040203	1.75E-07	1.173E-05	16.5	6.69
% gain	3.88	3.91	15.95	0.602	2.62

clinical metrics over the uniform porosity has also been reported in a previous work on a knee implant (Rahimizadeh et al., 2018). The rest of this section focuses on the comparison of the porous optimized implant with its fully-solid counterpart, as it is representative of the currently available implant in the market. Details on the importance of the respective clinical metrics are provided, along with a comprehensive comparison between the performance of the two implants.

Lower stress levels at the bone-implant interface are essential to provide initial implant stability and reduce the risk of interface debonding in the long-term. Additionally, in case of bone deficiency requiring bone grafts, lower stress levels on the acetabulum allow better maturation and incorporation of bone grafts and aid in bone graft remodeling (Kawanabe et al., 2011), which in turn contributes to the success of implant survival (Sembrano and Cheng, 2008). This work

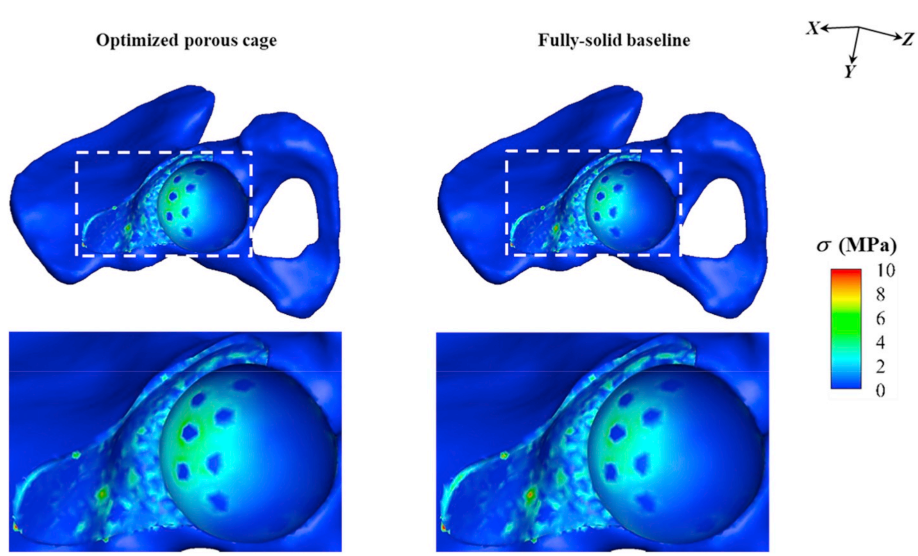

Fig. 4. Comparison of the contact total stress distribution at the bone-implant interface for fully-solid and fully-porous implants. The stress state includes both pressure and friction, and the distribution is plotted on the surface of the pelvic bone.

optimally tunes the elasticity of the implant through compliance-based optimization, which has been shown to be effective in reducing also the levels of interface stress (Moussa et al., 2018; Lin et al., 2004). As a comparison, the total contact stress distributions of the optimally porous cage and its fully-solid baseline are shown in Fig. 4. The former shows a better distribution with maximum peak of contact stress of 16.5 MPa; the latter, on the other hand, while showing a similar trend, features a 21 MPa peak stress. In particular, the fully-solid implant - as opposed to the optimized one - generates higher stress levels (mainly appearing in patches) on the ilium, with local concentrations in the middle and in the regions of contact with the implant edges. For both the implants, the bone tissue is almost unloaded on the acetabular regions close to the ischium and on the ilium regions farthest from the acetabulum. The 21.4% reduction of peak contact stress with the optimized cage (Fig. 4) indicates a considerable improvement in bone graft remodeling and host bone healing, factors that contribute to the long-term performance of the implant.

Micromotion at the bone-implant interface has been reported to affect bone ingrowth in the case of cementless fixation (Perona et al., 1992). Lower micromotion (typically below 28 μm) results in bone ingrowth, whereas excessive micromotion (above 150 μm) results in the growth of fibrous tissue, which inhibits biological fixation (Kienapfel et al., 1999). Bone-implant interface micromotion is largely dependent on the implant primary stability, which in turn depends on several factors. These include implant macro-geometry, elastic modulus mismatch with the bone, fixation technique as well as the quality of the host bone tissue and its defects (Rahimizadeh et al., 2018; Kienapfel et al., 1999). In this work, we focus on the reduction of the mismatch of elastic modulus with the bone tissue for given macro-geometry, mechanical fixation and bone tissue properties. Here, the micromotion is computed as the relative sliding distance between the bone and the implant surfaces. Fig. 5 illustrates the micromotion distribution on the bone surface for both the optimized cage and the fully-solid baseline. The former results in lower micromotion with a peak value of 6.69 μm, whereas the latter features a maximum value of 9.04 μm, with noticeably higher values of micromotion on the ilium. Furthermore, compared to the porous cage, the fully-solid one induces locally high micromotions along the implant flange edges. Although the peak micromotions are below the threshold for both cases, a further reduction of 26% with the optimized porous implant further contributes to its primary stability.

Adequate mechanical strength is essential to prevent structural failure of the porous cage here introduced. Fig. 6 shows the von Mises stress distributions for the optimized porous cage and the fully-solid implant. The results show lower von Mises stress distributions for the former with a maximum stress of 49.5 MPa, representing a 43% reduction from the fully-solid cage. This peak stress is well below the yield strength experimentally measured for the tetrahedron-based unit cell (Melancon et al., 2017), thereby validating its mechanical viability in this application. Additionally, the reduction in stresses contributes to prevent stress shielding and to provide a better load transfer to the surrounding bone tissue. This prevents bone resorption, which is essential for implant survival in the long-term.

As a preliminary proof-of-concept, the cage has been additively built with a photopolymer resin (FormLabs) using stereolithography (Formlabs, Somerville, Massachusetts, USA). Fig. 7 shows the 3D printed cage with a particular focus on the micro-architecture at two representative regions (Fig. 7A and B). Upon close visual inspection, the gradient of porosity can be easily observed, with thicker struts in regions of lower porosity and thinner struts in regions of higher porosity. The prototype generally retained the micro-architecture, with some defects, missing struts, arising from the 3D printing process as well as from the support removal. While this preliminary build demonstrates its manufacturability with a photopolymer resin, the next step involves the cage manufacturing via selective laser melting (SLM) with the Ti6Al4V alloy (Arabnejad et al., 2017). As demonstrated in previous studies on metallic implants, lattice structures made of Ti6Al4V have been successfully manufactured via SLM and experimentally tested with micro-architecture and graded porosity resembling those of the acetabular cage presented in this work (Arabnejad et al., 2017; Melancon et al., 2017).

Overall, the functionally graded fully-porous implant shows better clinical performance (lower contact stress and micromotion) compared to both the baselines. The gain over the fully-solid counterpart is significant (21.4% and 26% respectively), whereas that over the porous uniform one is relatively low. Such performance, i.e. stiffness, stress and micromotion, however, is expected to be further superior if a wider range of relative density could be used; the current range here used is a narrow one, as dictated by bone ingrowth and manufacturing requirements. Future improvement in additive manufacturing technology can potentially enable the fabrication of even finer struts, thereby enabling the use of wider range of relative density.

Despite the promising results of this numerical investigation, further work is required to address a number of limitations. First, a clinical loading case of one-legged standing is used for the analysis; however, the

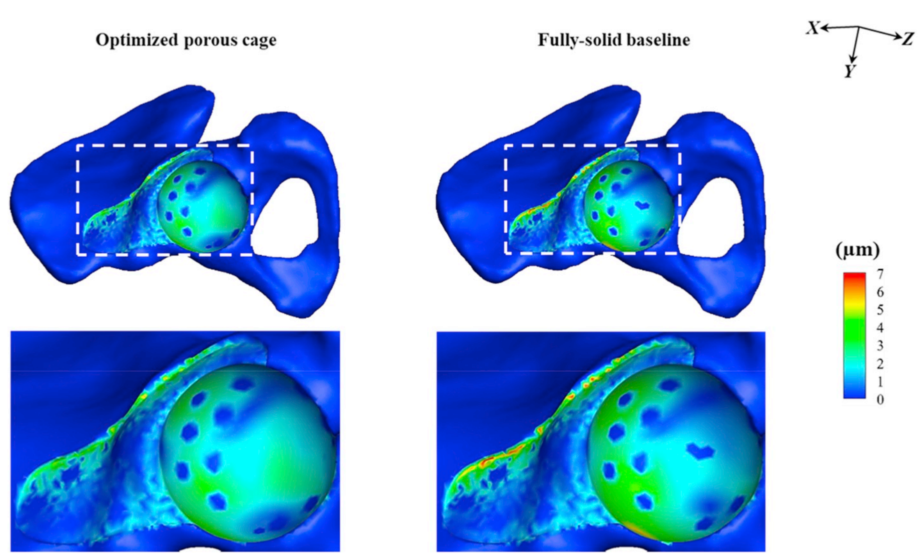

Fig. 5. Comparison of the micromotion distributions at the bone-implant interface for fully-solid and fully-porous implants. The distributions are plotted on the bone surface.

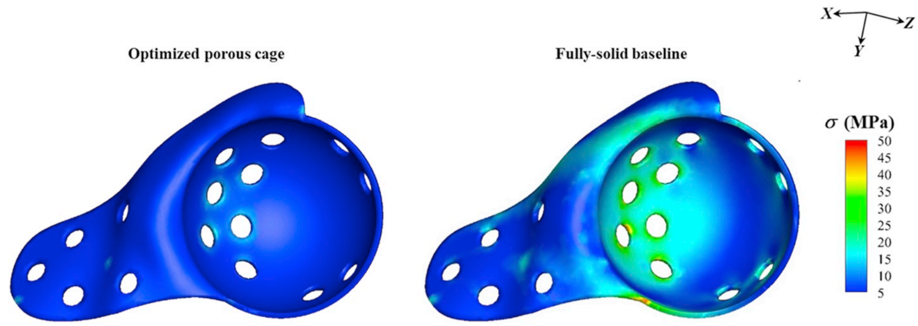

Fig. 6. Comparison of the von Mises stress distributions on the optimized porous implants and the fully-solid baseline. The stress distributions are shown for the face of the implant on which the load is applied.

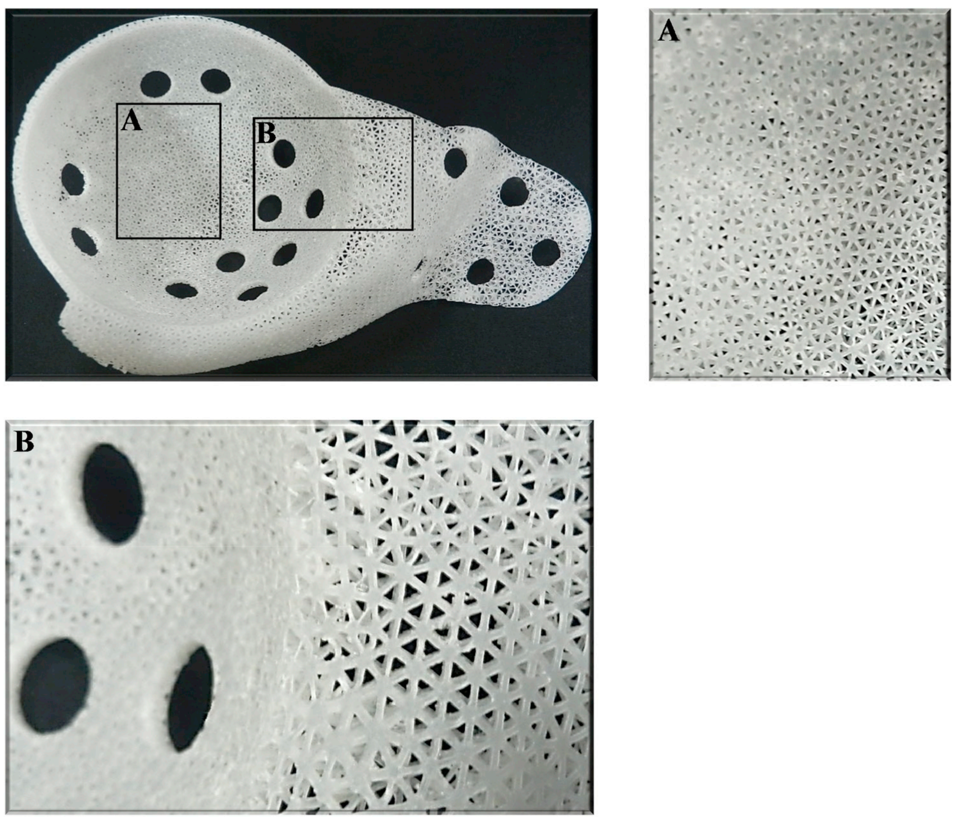

Fig. 7. Porous implant manufactured using a photopolymer resin as a proof-of-concept. Two regions are magnified to show the optimized variation in porosity.

performance of the cage under other loading scenarios, such as walking, running, and stair-climbing, need to be tested (Iqbal et al., 2019). In addition, fatigue and local stress constraints can be incorporated into the analysis and optimization scheme to further enhance the fatigue life of the implant. Another source of error comes from the manufacturing process. The lattice micro-architecture consists of strut thicknesses in microns that need to be manufactured with high fidelity to ensure biomechanical performance. Manufacturing induced imperfections, such as strut over-melting, of additively manufactured porous biomaterials can result in a shift of the design space of the unit cells (Arabnejad et al., 2016; Melancon et al., 2017). This can hamper the biomechanical performance of the implant and, hence, should be incorporated into the optimization framework. Lastly, the mechanical performance of the implant should be experimentally assessed in vitro and in vivo before clinical adoption.

4. Conclusions

This work has presented the numerical investigation of a novel pelvis cage design with a 3D-printed structurally porous architecture composed of high strength unit cells of optimally graded porosity. The design is expected to improve the clinical performance of current implants by lowering stress levels and micromotion at the bone-implant interface. Multiscale mechanics and density-based topology optimization have been systematically used to find the optimum gradient of porosity, and additive manufacturing has been used to fabricate a proof-of-concept of the fairly complex micro-architecture. The additive manufacturing requirements are incorporated into the optimization scheme via inclusion of heat-treated, additively manufactured titanium alloy material properties and requirements on the minimum manufacturable strut thickness.

The numerical results indicate that the porous implant leads to a 21.4% reduction in the maximum stress on the bone surface and a 26%

decrease in the peak micromotion at the bone-implant interface compared to its fully-solid counterpart. The low stress levels shield the acetabulum from detrimental high level of stress and allow host bone healing before bone ingrowth can occur, in addition the lower initial micromotion enhances bone ingrowth and biological fixation. This reduces the risk of interface debonding and aides in long-term implant stability. The numerical results here presented are indicators of significant functional improvements that warrant further experimental and clinical validation in the near future.

Declaration of competing interest

The authors declare that they have no known competing financial interests or personal relationships that could have appeared to influence the work reported in this paper.

CRediT authorship contribution statement

Ahmed Moussa: Conceptualization, Formal analysis, Methodology, Software, Validation, Writing - original draft, Writing - review & editing. **Shakurur Rahman:** Formal analysis, Methodology, Software, Validation, Writing - original draft, Writing - review & editing. **Manman Xu:** Methodology. **Michael Tanzer:** Conceptualization. **Damiano Pasini:** Conceptualization, Methodology, Supervision, Writing - original draft, Writing - review & editing, Funding acquisition.

Acknowledgements

The authors acknowledge funding from the Natural Sciences and Engineering Research Council of Canada through the Discovery Grant Program and the Network for Holistic Innovation in Additive Manufacturing.

References

Abbas, R.S., Al Ali, M., Sahib, A.Y., 2018. Designing femoral implant using stress based topology optimization. In: Proceedings of the World Congress on Engineering, vol. 1.
Al-Tamimi, A.A., Peach, C., Fernandes, P.R., Cseke, A., Bartolo, P.J., 2017. Topology Optimization to reduce the stress shielding effect for orthopedic applications. Procedia CIRP 65, 202–206.
Arabnejad, S., Pasini, D., 2013. Mechanical properties of lattice materials via asymptotic homogenization and comparison with alternative homogenization methods. Int. J. Mech. Sci. 77, 249–262.
Arabnejad, S., Johnston, R.B., Pura, J.A., Singh, B., Tanzer, M., Pasini, D., 2016. High-strength porous biomaterials for bone replacement: a strategy to assess the interplay between cell morphology, mechanical properties, bone ingrowth and manufacturing constraints. Acta Biomater. 30, 345–356.
Arabnejad, S., Johnston, B., Tanzer, M., Pasini, D., 2017. Fully porous 3D printed titanium femoral stem to reduce stress-shielding following total hip arthroplasty. J. Orthop. Res. 35 (8), 1774–1783.
Arabnejad Khanoki, S., Pasini, D., 2012. Multiscale design and multiobjective optimization of orthopedic hip implants with functionally graded cellular material. J. Biomech. Eng. 134 (3).
Bendsøe, M.P., Sigmund, O., 2003. Topology Optimization : Theory, Methods, and Applications. Springer, Berlin; New York in English.
Bobyn, J., Pilliar, R., Cameron, H., Weatherly, G., 1980. The optimum pore size for the fixation of porous-surfaced metal implants by the ingrowth of bone. Clin. Orthop. Relat. Res. (150), 263–270.
Bobyn, J., Stackpool, G., Hacking, S., Tanzer, M., Krygier, J., 1999. Characteristics of bone ingrowth and interface mechanics of a new porous tantalum biomaterial. J. Bone Jt. Surg. Br. Vol. 81 (5), 907–914.
Bose, S., Vahabzadeh, S., Bandyopadhyay, A., 2013. Bone tissue engineering using 3D printing. Mater. Today 16 (12), 496–504.
Bruns, T.E., Tortorelli, D.A., 2001. Topology optimization of non-linear elastic structures and compliant mechanisms. Comput. Methods Appl. Mech. Eng. 190 (26–27), 3443–3459.
Cignoni, P., Callieri, M., Corsini, M., Dellepiane, M., Ganovelli, F., Ranzuglia, G., 2008. Meshlab: an open-source mesh processing tool. In: Eurographics Italian Chapter Conference, vol. 2008, pp. 129–136.
Crawford, R.P., Cann, C.E., Keaveny, T.M., 2003. Finite element models predict in vitro vertebral body compressive strength better than quantitative computed tomography. Bone 33 (4), 744–750.
Dall'Ava, L., Hothi, H., Di Laura, A., Henckel, J., Hart, A., 2019. 3D printed acetabular cups for total hip arthroplasty: a review article. Metals 9 (7), 729.
Dalstra, M., Huiskes, R., Odgaard, A.v., Van Erning, L., 1993. Mechanical and textural properties of pelvic trabecular bone. J. Biomech. 26 (4–5), 523–535.
Dalstra, M., Huiskes, R., Van Erning, L., 1995. Development and Validation of a Three-Dimensional Finite Element Model of the Pelvic Bone.
Dearborn, J.T., Harris, W.H., 1999. High placement of an acetabular component inserted without cement in a revision total hip arthroplasty. Results after a mean of ten years. J. Bone Joint Surg. 81 (4), 469–480.
Fang, Z., Starly, B., Sun, W., 2005. Computer-aided characterization for effective mechanical properties of porous tissue scaffolds. Comput. Aided Des. 37 (1), 65–72.
FormLabs. Materials Data Sheet [Online] Available. http://uprint3d.xyz/media/material_data/XL-DataSheet.pdf.
Fraldi, M., Esposito, L., Perrella, G., Cutolo, A., Cowin, S., 2010. Topological optimization in hip prosthesis design. Biomech. Model. Mechanobiol. 9 (4), 389–402.
Gross, A.E., Goodman, S.B., 2005. Rebuilding the skeleton: the intraoperative use of trabecular metal in revision total hip arthroplasty. J. Arthroplasty 20, 91–93.
Hao, Z., Wan, C., Gao, X., Ji, T., 2011. The effect of boundary condition on the biomechanics of a human pelvic joint under an axial compressive load: a three-dimensional finite element model. J. Biomech. Eng. 133 (10), 101006.
Hassani, B., 1996. A direct method to derive the boundary conditions of the homogenization equation for symmetric cells. Commun. Numer. Methods Eng. 12 (3), 185–196.
Hassani, B., Hinton, E., 1998. A review of homogenization and topology optimization I—homogenization theory for media with periodic structure. Comput. Struct. 69 (6), 707–717.
Hendricks, K.J., Harris, W.H., 2006. Revision of failed acetabular components with use of so-called jumbo noncemented components: a concise follow-up of a previous report. J. Bone Joint Surg. 88 (3), 559–563.
Hirst, P., Esser, M., Murphy, J., Hardinge, K., 1987. Bone grafting for protrusio acetabuli during total hip replacement. A review of the Wrightington method in 61 hips. J. Bone Jt. Surg. Br. Vol. 69 (2), 229–233.
Hoell, S., Dedy, N., Gosheger, G., Dieckmann, R., Daniilidis, K., Hardes, J., 2012. The Burch–Schneider cage for reconstruction after metastatic destruction of the acetabulum: outcome and complications. Arch. Orthop. Trauma Surg. 132 (3), 405–410.
Hollister, S.J., Kikuchi, N., 1992. A comparison of homogenization and standard mechanics analyses for periodic porous composites. Comput. Mech. 10 (2), 73–95.
Huiskes, R., Weinans, H., Van Rietbergen, B., 1992. The relationship between stress shielding and bone resorption around total hip stems and the effects of flexible materials. Clin. Orthop. Relat. Res. 124–134.
Iqbal, T., Wang, L., Li, D., Dong, E., Fan, H., Fu, J., Hu, C., 2019. A general multi-objective topology optimization methodology developed for customized design of pelvic prostheses. Med. Eng. Phys. 69, 8–16.
Ito, H., Matsuno, T., Aoki, Y., Minami, A., 2003. Acetabular components without bulk bone graft in revision surgery:: a 5-to 13-year follow-up study. J. Arthroplasty 18 (2), 134–139.
Jasty, M., Bragdon, C., Burke, D., O'Connor, D., Lowenstein, J., Harris, W.H., 1997. In vivo skeletal responses to porous-surfaced implants subjected to small induced motions. J. Bone Joint Surg. 79 (5), 707–714.
Katoozian, H., Davy, D.T., Arshi, A., Saadati, U., 2001. Material optimization of femoral component of total hip prosthesis using fiber reinforced polymeric composites. Med. Eng. Phys. 23 (7), 505–511.
Kawanabe, K., Akiyama, H., Onishi, E., Nakamura, T., 2007. Revision total hip replacement using the Kerboull acetabular reinforcement device with morsellised or bulk graft: results at a mean follow-up of 8.7 years. J. Bone Jt. Surg. Br. Vol. 89 (1), 26–31.
Kawanabe, K., Akiyama, H., Goto, K., Maeno, S., Nakamura, T., 2011. Load dispersion effects of acetabular reinforcement devices used in revision total hip arthroplasty: a simulation study using finite element analysis. J. Arthroplasty 26 (7), 1061–1066.
Khanoki, S.A., Pasini, D., 2013. Fatigue design of a mechanically biocompatible lattice for a proof-of-concept femoral stem. J. Mech. Behav. Biomed. Mater. 22, 65–83.
Kienapfel, H., Sprey, C., Wilke, A., Griss, P., 1999. Implant fixation by bone ingrowth. J. Arthroplasty 14 (3), 355–368.
Lengsfeld, M., Schmitt, J., Alter, P., Kaminsky, J., Leppek, R., 1998. Comparison of geometry-based and CT voxel-based finite element modelling and experimental validation. Med. Eng. Phys. 20 (7), 515–522.
Leung, A., Gordon, L., Skrinskas, T., Szwedowski, T., Whyne, C., 2009. Effects of bone density alterations on strain patterns in the pelvis: application of a finite element model. Proc. IME H J. Eng. Med. 223 (8), 965–979.
Levine, B., 2008. A new era in porous metals: applications in orthopaedics. Adv. Eng. Mater. 10 (9), 788–792.
Lin, C.-Y., Hsiao, C.-C., Chen, P.-Q., Hollister, S.J., 2004. Interbody fusion cage design using integrated global layout and local microstructure topology optimization. Spine 29 (16), 1747–1754.
Ma, W., Zhang, X., Wang, J., Zhang, Q., Chen, W., Zhang, Y., 2013. Optimized design for a novel acetabular component with three wings. A study of finite element analysis. J. Surg. Res. 179 (1), 78–86.
Melancon, D., Bagheri, Z., Johnston, R., Liu, L., Tanzer, M., Pasini, D., 2017. Mechanical characterization of structurally porous biomaterials built via additive manufacturing: experiments, predictive models, and design maps for load-bearing bone replacement implants. Acta Biomater. 63, 350–368.
Mendes, D.G., Roffman, M., Silbermann, M., 1984. Reconstruction of the acetabular wall with bone graft in arthroplasty of the hip. Clin. Orthop. Relat. Res. (186), 29–37.
Moore, K.D., McClenny, M.D., Wills, B.W., 2018. Custom triflange acetabular components for large acetabular defects: minimum 10-year follow-up. Orthopedics 41 (3), e316–e320.

Morgan, E.F., Bayraktar, H.H., Keaveny, T.M., 2003. Trabecular bone modulus–density relationships depend on anatomic site. J. Biomech. 36 (7), 897–904.

Moussa, A., Tanzer, M., Pasini, D., 2018. Cervical fusion cage computationally optimized with porous architected Titanium for minimized subsidence. J. Mech. Behav. Biomed. Mater. 85, 134–151.

Murr, L.E., Gaytan, S., Medina, F., Lopez, H., Martinez, E., Machado, B., Hernandez, D., Martinez, L., Lopez, M., Wicker, R., 2010. Next-generation biomedical implants using additive manufacturing of complex, cellular and functional mesh arrays. Phil. Trans. Math. Phys. Eng. Sci. 368 (1917), 1999–2032.

Odgaard, A., 1997. Three-dimensional methods for quantification of cancellous bone architecture. Bone 20 (4), 315–328.

Padgett, D.E., Kull, L., Rosenberg, A., Sumner, D.R., Galante, J.O., 1993. Revision of the acetabular component without cement after total hip arthroplasty. Three to six-year follow-up. J. Bone Jt. Surg. Am. Vol. 75 (5), 663–673.

Paprosky, W.G., Magnus, R.E., 1994. Principles of bone grafting in revision total hip arthroplasty. Acetabular technique. Clin. Orthop. Relat. Res. (298), 147–155.

Paprosky, W.G., Perona, P.G., Lawrence, J.M., 1994. Acetabular defect classification and surgical reconstruction in revision arthroplasty: a 6-year follow-up evaluation. J. Arthroplasty 9 (1), 33–44.

Patel, J., Masonis, J., Bourne, R., Rorabeck, C., 2003. The fate of cementless jumbo cups in revision hip arthroplasty. J. Arthroplasty 18 (2), 129–133.

Peng, L., Bai, J., Zeng, X., Zhou, Y., 2006. Comparison of isotropic and orthotropic material property assignments on femoral finite element models under two loading conditions. Med. Eng. Phys. 28 (3), 227–233.

Perka, C., Ludwig, R., 2001. Reconstruction of segmental defects during revision procedures of the acetabulum with the Burch-Schneider anti-protrusio cage. J. Arthroplasty 16 (5), 568–574.

Perona, P.G., Lawrence, J., Paprosky, W.G., Patwardhan, A.G., Sartori, M., 1992. Acetabular micromotion as a measure of initial implant stability in primary hip arthroplasty: an in vitro comparison of different methods of initial acetabular component fixation. J. Arthroplasty 7 (4), 537–547.

Pollock, F.H., Whiteside, L.A., 1992. The fate of massive allografts in total hip acetabular revision surgery. J. Arthroplasty 7 (3), 271–276.

Rahimizadeh, A., Nourmohammadi, Z., Arabnejad, S., Tanzer, M., Pasini, D., 2018. Porous architected biomaterial for a tibial-knee implant with minimum bone resorption and bone-implant interface micromotion. J. Mech. Behav. Biomed. Mater. 78, 465–479.

Rho, J.-Y., Hobatho, M., Ashman, R., 1995. Relations of mechanical properties to density and CT numbers in human bone. Med. Eng. Phys. 17 (5), 347–355.

Rosson, J., Schatzker, J., 1992. The use of reinforcement rings to reconstruct deficient acetabula. J. Bone Jt. Surg. Br. Vol. 74 (5), 716–720.

Schutzer, S.F., Harris, W.H., 1994. High placement of porous-coated acetabular components in complex total hip arthroplasty. J. Arthroplasty 9 (4), 359–367.

Sembrano, J.N., Cheng, E.Y., 2008. Acetabular cage survival and analysis of factors related to failure. Clin. Orthop. Relat. Res. 466 (7), 1657–1665.

Sobral, J.M., Caridade, S.G., Sousa, R.A., Mano, J.F., Reis, R.L., 2011. Three-dimensional plotted scaffolds with controlled pore size gradients: effect of scaffold geometry on mechanical performance and cell seeding efficiency. Acta Biomater. 7 (3), 1009–1018.

Svanberg, K., 1987. The method of moving asymptotes—a new method for structural optimization. Int. J. Numer. Methods Eng. 24 (2), 359–373.

Symeonides, P.P., Petsatodes, G.E., Pournaras, J.D., Kapetanos, G.A., Christodoulou, A. G., Marougiannis, D.J., 2009. The effectiveness of the Burch-Schneider antiprotrusio cage for acetabular bone deficiency: five to twenty-one years' follow-up. J. Arthroplasty 24 (2), 168–174.

Viceconti, M., Bellingeri, L., Cristofolini, L., Toni, A., 1998. A comparative study on different methods of automatic mesh generation of human femurs. Med. Eng. Phys. 20 (1), 1–10.

Wang, X., Xu, S., Zhou, S., Xu, W., Leary, M., Choong, P., Qian, M., Brandt, M., Xie, Y.M., 2016. Topological design and additive manufacturing of porous metals for bone scaffolds and orthopaedic implants: a review. Biomaterials 83, 127–141.

Wang, Y., Xu, H., Pasini, D., 2017. Multiscale isogeometric topology optimization for lattice materials. Comput. Methods Appl. Mech. Eng. 316, 568–585.

Wang, Y., Arabnejad, S., Tanzer, M., Pasini, D., 2018. Hip implant design with three-dimensional porous architecture of optimized graded density. J. Mech. Des. 140 (11), 111406.

Winter, E., Piert, M., Volkmann, R., Maurer, F., Eingartner, C., Weise, K., Weller, S., 2001. Allogeneic cancellous bone graft and a Burch-Schneider ring for acetabular reconstruction in revision hip arthroplasty. J. Bone Joint Surg. 83 (6), 862–867.

Yang, K.-H., 2017. Basic Finite Element Method as Applied to Injury Biomechanics. Academic Press.

Yushkevich, P.A., Piven, J., Hazlett, H.C., Smith, R.G., Ho, S., Gee, J.C., Gerig, G., 2006. User-guided 3D active contour segmentation of anatomical structures: significantly improved efficiency and reliability. Neuroimage 31 (3), 1116–1128.